Monte Carlo Method for Uncertainty Propagation in Magnetic Resonance-Based Electric Properties Tomography

Monte Carlo method for uncertainty propagation in magnetic resonance-based electric properties tomography

Authors

Alessandro Arduino[a,b], Mario Chiampi[a], Francesca Pennechi[b], Luca Zilberti[b], Oriano Bottauscio[b]

Author affiliation

[a] Dipartimento Energia – Politecnico di Torino – Corso Duca degli Abruzzi, 24 – 10129 Torino, Italia

[b] Istituto Nazionale di Ricerca Metrologica (INRIM) – Strada delle Cacce, 91 – 10135 Torino, Italia

* Correspondence should be addressed to: alessandro.arduino@polito.it

Published journal article available at DOI: https://doi.org/10.1109/TMAG.2017.2713984

Monte Carlo Method for Uncertainty Propagation in Magnetic Resonance-based Electric Properties Tomography

Alessandro Arduino[1,2], Mario Chiampi[1], Francesca Pennecchi[2], Luca Zilberti[2], and Oriano Bottauscio[2]

[1]Dipartimento Energia, Politecnico di Torino, 10129 Torino, Italy
[2]Istituto Nazionale di Ricerca Metrologica, 10135 Torino, Italy

This paper investigates the uncertainty propagation in magnetic resonance-based electric properties tomography, a quantitative imaging technique that recovers the electric properties distribution inside a human body at the Larmor frequency. This is a needed step in order to make the quantitative results reliable for *in vivo* applications. To this aim, the contrast source inversion method is investigated as a promising technique and the uncertainty propagation through the corresponding model is studied by means of the Monte Carlo method. Thanks to the increased quality in the recovered electric properties, the results suggest that TEM coils for parallel transmission could be a preferable choice.

***Index Terms*—Electric properties tomography, magnetic resonance imaging, contrast source inversion, uncertainty propagation, Monte Carlo method.**

I. Introduction

Quantitative tomography, namely the possibility to generate images of the inside of a human body whose pixels are measurements of some physical parameters, aroused an increasing interest in the last years. For example, images of the mechanical properties of biological tissues provided by magnetic resonance elastography has proven to be a useful diagnostic tool replacing palpation in clinical routine [1]. Also, there are expectations on the impact of magnetic resonance fingerprinting, which leads to images of relaxation times, proton density and other parameters involved in magnetic resonance imaging (MRI) [2].

Among the techniques proposed in literature to investigate the imaging of the electric properties (permittivity and conductivity) of biological tissues at low frequency [3, 4] and radiofrequency (RF) [5-7], this paper focuses on the magnetic resonance-based electric properties tomography (MREPT). This strategy, formerly proposed in [6] and rediscovered in recent years [7], recovers the electric properties from the RF magnetic field measurements obtained by B1-mapping techniques [8]. The application of the contrast source inversion technique to MREPT (CSI-EPT) [9, 10] leads to the additional recovery of a map of the whole RF electromagnetic field [11, 12]. Thus, it is of particular interest in MRI safety, where patient-specific estimation of the local specific absorption rate is needed. Unlike standard MREPT strategies [13], CSI-EPT currently lacks of an uncertainty assessment, necessary to make the method reliable for *in vivo* applications. This paper investigates the noise propagation in CSI-EPT applying the Monte Carlo method (MCM), in accordance to the Supplement 1 to GUM (Guide to the expression of Uncertainty in Measurement) on the propagation of probability distributions [14].

II. Methods

A. CSI-EPT with multiple settings

B1-mapping techniques can measure the positively rotating component of the magnetic field generated by RF coils $B_1^+=(B_{1,x}+\mathrm{i}B_{1,y})/2$ [8, 15] (with a neglected systematic error in phase estimation that gets sensible at frequencies above 128 MHz [15]), where $B_{1,x}$ and $B_{1,y}$ denote the Cartesian components transverse to the static field $\mathbf{B}_0$. Based on this measurement and on the knowledge of the electromagnetic field generated by the RF coil in absence of the investigated body (incident field), the CSI-EPT method solves an optimal control problem by minimising a cost functional F with respect to the contrast $\chi = (\varepsilon-\mathrm{i}\sigma/\omega)/(\varepsilon_\mathrm{b}-\mathrm{i}\sigma_\mathrm{b}/\omega)-1$ and the contrast source $\mathbf{w} = \chi\mathbf{E}$. In these relations, written assuming phasor notation at Larmor frequency $\omega/(2\pi)$ with convention $\mathrm{e}^{\mathrm{i}\omega t}$, ε is the electric permittivity, σ is the electric conductivity, subscript b denotes the background properties and $\mathbf{E}$ is the electric field generated by the coil in presence of the investigated body (total field). The electric properties are obtained from the real and imaginary parts of χ, the actual unknown of CSI-EPT, whereas $\mathbf{w}$ is an auxiliary unknown.

It is possible to incorporate a number J of measurements from multiple coil settings in the CSI-EPT method by defining the cost functional [9]

$$F[(\mathbf{w}_j)_{j=1}^J,\chi]=\frac{\sum_{j=1}^J\left\|\rho_j[\mathbf{w}_j]\right\|^2}{2\sum_{j=1}^J\left\|B_{1,j}^{+;\mathrm{s}}\right\|^2}+\frac{\sum_{j=1}^J\left\|\mathbf{r}_j[\mathbf{w}_j,\chi]\right\|^2}{2\sum_{j=1}^J\left\|\chi\mathbf{E}_j^{\mathrm{i}}\right\|^2}, \qquad (1)$$

where $B_{1,j}^{+;\mathrm{s}}$ is the scattered part of the B_1^+ map of the j-th coil setting (evaluated only inside the investigated body), $\mathbf{E}_j^{\mathrm{i}}$ is the incident electric field generated by the j-th source, and ρ_j and $\mathbf{r}_j$ are the data and the state residuals defined as in [10].

A two-step alternating conjugate-gradient method with Polak-Ribière directions is used to implement numerically the minimisation of (1) [16]. Precisely, assuming known values of contrast χ^{n-1} and contrast source $\mathbf{w}_j^{n-1}$ for each coil setting j, the contrast sources are updated first with the scheme

$$\mathbf{w}_j^n=\mathbf{w}_j^{n-1}+\alpha^{n-1}\mathbf{v}_j^{n-1}, \qquad (2)$$

where $\mathbf{v}_j^{n-1}$ is the Polak-Ribière direction computed by means of the gradient of the cost function with respect to the j-th

Fig. 1. Considered section of the head.

contrast source [10], and α^{n-1} is the real step length that minimises $F[(\mathbf{w}_j^{n-1}+\alpha^{n-1}\mathbf{v}_j^{n-1})_{j=1}^{J}, \chi^{n-1}]$. Parameter α^{n-1} has an analytical expression in closed form [10, 16]. Then, the j-th contrast source provides an estimate $\mathbf{E}_j^{n-1}$ of the total electric field $\mathbf{E}_j$, which is used in the contrast update [10, 16]

$$\chi^n = \frac{\sum_{j=1}^{J} \mathbf{w}_j^n \cdot \bar{\mathbf{E}}_j^n}{\sum_{j=1}^{J} \left|\mathbf{E}_j^n\right|^2}. \qquad (3)$$

The iterative procedure starts with (3) evaluated at the initial guess for the contrast sources chosen by backpropagation [10].

The knowledge of the region occupied by the body (easily inferable from MRI output) gives rise to a convex constraint on the contrast that is implemented by projection, together with a positivity constraint for the electric properties [10].

B. *Monte Carlo method*

In order to study the uncertainty propagation in CSI-EPT by means of the MCM [14], the inversion procedure is applied to a two-dimensional model problem in which virtual measurements are given by numerical simulations. Precisely, the solution of Maxwell's equations provides both the incident and the total actual fields generated by certain coils. To simulate the measurement uncertainty, additive Gaussian noise is introduced to the total field only. Indeed, the uncertainty in the incident field can be precisely supervised, because its evaluation is performed just once before any other measurement, and so it can reasonably be expected that B1-mapping plays a dominant role in noise propagation.

Noise extracted according to a Gaussian distribution with null mean and constant standard deviation u is added to both the real and the imaginary part of each pixel of the simulated B_1^+ map. So, spatially uncorrelated noise has been adopted. The standard deviation of the noise is defined in terms of the spatially averaged signal to noise ratio (SNR), as it is usual in imaging. For any specific probability distribution, SNR means the ratio between its mean value and its standard deviation. In the following, SNR distributions evaluated pixel-by-pixel are referred to as local SNR. The data corrupted in this way are elaborated by CSI-EPT for a given number of iterations.

For each configuration of the involved parameters, the MCM has been applied on just 1000 trials, a smaller number than that indicated in [14], because of the relevant computational cost of the inversion procedure. In this way, as can be seen in the following histograms, probability distributions with a small variance are estimated more precisely than those with higher variance, the latter still being qualitatively recognisable, however. The spatial distributions of relative permittivity and electric conductivity resulting from the different trials are collected and elaborated in statistics according to [14]. No investigation has been performed for the uncertainty in contrast sources estimation.

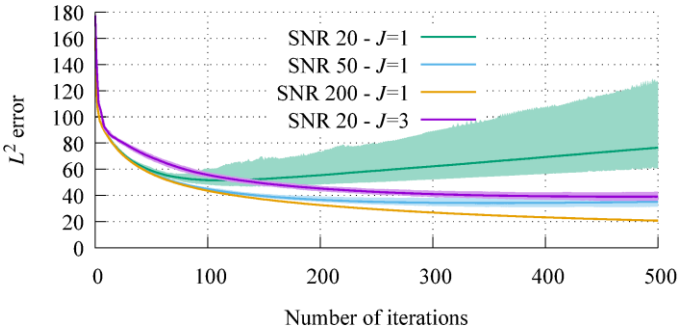

Fig. 2. Trend of the median (solid lines) and shortest 95 % coverage interval (bands) of the L^2 norm of the error in χ against the number of iterations of CSI-EPT for different SNR and coil settings. The 16 legs birdcage is considered.

III. Results and Discussion

The analysis concerns a transverse section of the head of the anatomical human model Duke of the Virtual Family [17], segmented with a resolution of 2 mm (Fig. 1). The properties of the biological tissues are collected in the database of IT'IS Foundation [18]. The radiation of the body with a birdcage and some TEM coils of diameter 28.0 cm is modelled with transverse magnetic (TM) assumption. The coils are driven at 128 MHz (Larmor frequency for a 3 T scanner). In all cases, the coils are assumed to be unshielded [10].

A. *Birdcage coil*

A 16 legs birdcage coil is approximated by 16 line sources uniformly distributed on a circle and numbered clockwise by the index k = 0, …, 15. For a birdcage coil, it is possible to distinguish between two linear excitations, whose currents exhibit a spatial phase shift of 90°,

$$I_k^{l_1} = \cos(\varphi_k), \qquad I_k^{l_2} = \sin(\varphi_k), \qquad (4)$$

and a quadrature excitation obtained by combining the linear excitations with a time delay of a quarter of period,

$$I_k^{q} = I_k^{l_1} + \mathrm{i} I_k^{l_2}. \qquad (5)$$

Fig. 2 represents the stochastic behaviour of the L^2 norm of the error of the recovered contrast with respect to the actual value when CSI-EPT is applied to the virtual measurements obtained from quadrature excitation only (J = 1) and from all the three excitations (J = 3). The statistics are computed on the results obtained by the MCM. The trend of the median of the error is characteristic of an ill-posed problem, because it reaches a minimum after a certain finite number of iterations and then increases, as it is particularly evident for the green line. In addition, the error has an almost deterministic behaviour in the first iterations (coverage intervals are very short), but getting close to the minimum the randomness appears and increases together with the number of iterations. It is worth noting that the trend of the error with J = 3 is substantially different from the trends with J = 1, starting from

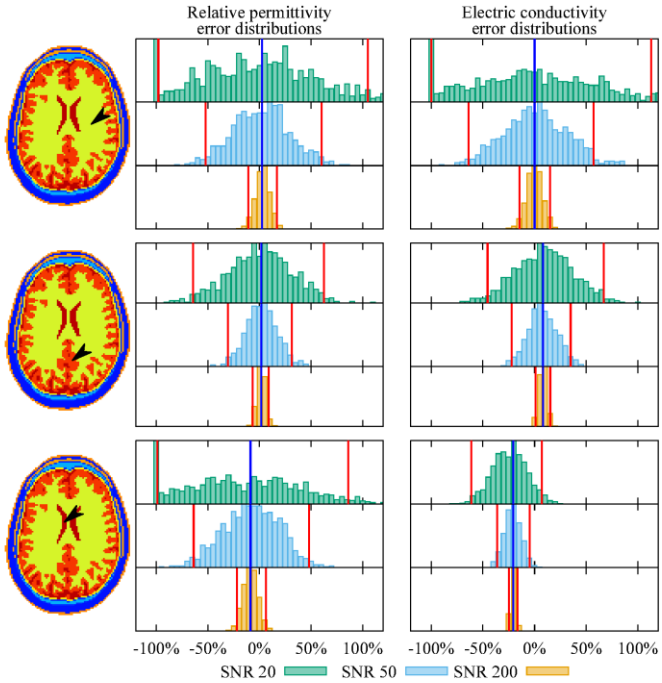

Fig. 3. Relative frequency histograms of electric properties relative errors after 300 iterative steps in some inner pixels identified by arrows in the maps on the left. Different amount of noise are considered for a 16 legs birdcage in quadrature excitation. The vertical blue lines denote the relative errors in absence of noise (intrinsic bias); the vertical red lines indicate the shortest 95 % coverage intervals.

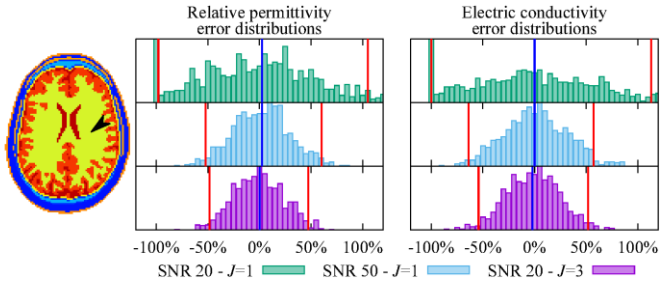

Fig. 4. Relative frequency histograms of electric properties relative errors after 300 iterative steps in the inner pixel identified by the arrow in the map on the left. A 16 legs birdcage coil is considered with different coil settings and different amount of noise. The vertical blue lines denote the relative errors in absence of noise; the vertical red lines indicate the shortest 95 % coverage intervals.

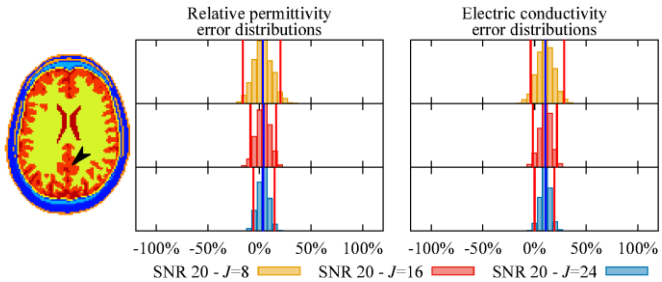

Fig. 5. Relative frequency histograms of properties relative errors after 60 iterative steps in the inner pixel identified by the arrow in the map on the left. Different TEM coils are considered. The vertical blue lines denote the relative errors in absence of noise; the vertical red lines indicate the shortest 95 % coverage intervals.

the very first (deterministic) iterative steps. This happens because the cost functional explicitly depends on J and so the two cases tread different minimisation paths independently of the noise. Moreover, although the amount of noise is higher, the behaviour of the purple line (SNR 20 and J = 3) is very similar to that of the blue line (SNR 50 and J = 1), suggesting an improvement due to the adoption of multiple coil settings.

Relative frequency histograms in Fig. 3 show, for some inner pixels, the distributions of local relative errors in the electric properties obtained after 300 iterative CSI-EPT steps with the quadrature excitation only (J = 1). It is worth noting that such number of iterative steps locate themselves around the minimum global error for SNR 50, in the decreasing region for SNR 200, and in the increasing, highly stochastic region for SNR 20 (Fig. 2). As expected, higher uncertainties in the input correspond to higher uncertainties in the output. However, uncertainty shows a sensible spatial dependency. The discrete distributions are quite symmetric except for some cases with SNR 20, whose distributions are so wide to suffer from the positivity constraint of CSI-EPT and exhibit an anomalous peak at -100 %. Moreover, the distributions are not centred on 0 %, but they show a bias that does not depend on the amount of noise in the input. Precisely, this intrinsic bias coincides with the local relative error achieved by applying 300 steps of CSI-EPT to the noise-free input.

The results are improved by adopting all the three coil settings for the reconstruction. The histograms in Fig. 4 show how the coverage intervals for SNR 20 and J = 3 (purple histogram) are narrower with respect to J = 1, even for SNR 50. Quantitatively, the averaged SNR of the recovered relative permittivity is 9 times less than the input SNR for J = 1 and 3 times less for J = 3; output electric conductivity shows a spatially averaged SNR 7 times less than the input for J = 1 and 2.3 times less for J = 3.

B. TEM coil

TEM coils are very similar to birdcage coils, but have the main advantage of driving each leg independently. This result is achieved by disposing a second circle of returning line sources 2 cm larger than the one already described for the birdcage coil, and considering one coil setting for each couple of lines. In case of a TEM coil with J legs, numbered clockwise by the index k = 0, …, J-1, the j-th coil setting is obtained by exciting the inner circle with

$$I_k^{\mathrm{TEM},j} = \delta_{k,j} e^{i\frac{2\pi k}{J}}, \qquad (6)$$

and the outer circle with $-I_k^{\mathrm{TEM},j}$. Symbol $\delta_{k,j}$ denotes the Kronecker delta function.

TEM coils with 8, 16, and 24 legs have been considered. In all the cases, a global error comparable to that obtained for the birdcage coil after 300 iterative steps is reached with 60 steps. Fig. 5 collects the distributions of the electric properties after 60 steps. As expected, the length of the coverage intervals is strongly reduced with respect to the birdcage coil studies while maintaining almost the same bias, which again coincides with the intrinsic bias resulting by application of 60 steps of CSI-EPT to the noise-free input. The spatially averaged SNR of both the electric properties increases with the number of legs of the coil and results to be very close to the input SNR for all the considered cases.

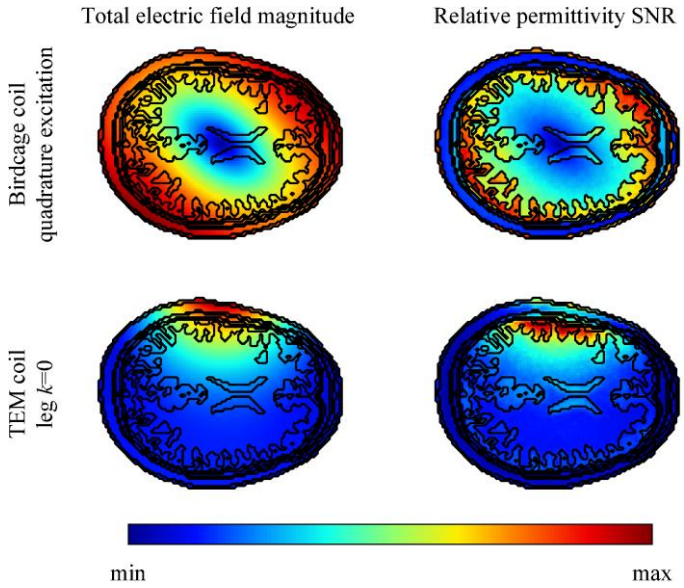

Fig. 6. Color maps of the total electric field (left column) and of the local SNR in the relative permittivity recovered by CSI-EPT (right column) for a birdcage coil in quadrature excitation and for one leg of a TEM coil. Black lines identify the borders of the tissues.

In addition, by applying CSI-EPT to maps of TEM coils, the known issue in local reconstruction of the properties in the region of minimum total electric field [9, 10] is completely solved. From a statistical viewpoint, this issue can be related to the local uncertainty of the recovery, which becomes very high (low SNR) where the electric field magnitude is low, as can be inferred from the maps in Fig. 6 (the region of bone has low SNR because of very low ε). Some analyses, not presented here, show that a spatially homogeneous uncertainty in the input (as used in all the simulations) is propagated to an almost spatially homogeneous uncertainty both in the contrast sources and in the estimated total electric fields. Thus, in points where the electric field is low, equation (3) is more sensitive to the uncertainty and leads to less accurate reconstruction of the contrast. As can be seen in Fig. 7, the issue cannot be solved by using the three excitations of the birdcage coil, but it completely disappears with the TEM coil.

IV. Conclusion

In this work, the uncertainty propagation in a quantitative imaging technique that recovers the electric properties distribution inside a human body by minimising a non-linear cost functional is studied by means of the MCM.

The results suggest that the accuracy of the recovered electric properties is improved by the adoption of multiple coil settings. In particular, thanks to the low number of required iterative steps, high SNR in the results, and absence of the issue related to the minimum electric field, TEM coils appear to be the preferable choice for application of CSI-EPT.

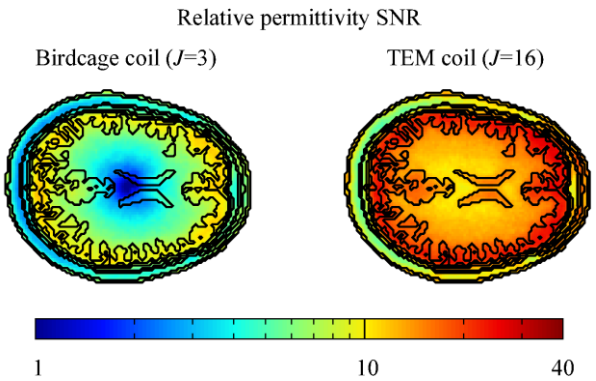

Fig. 7. Local SNR of relative permittivity recovered by CSI-EPT from noisy data (SNR 20) obtained from a birdcage with 3 coil settings and a TEM coil with 16 legs. Logarithmic scale. Black lines identify the borders of the tissues.

References

[1] L. V. Hiscox, *et al*, "Magnetic resonance elastography (MRE) of the human brain: technique, findings and clinical applications," *Phys. Med. Biol.*, vol. 61, no. 24, pp. R401-R437, Nov 2016.

[2] European Society of Radiology (ESR), "Magnetic resonance fingerprinting – a promising new approach to obtain standardized imaging biomarkers from MRI," *Insights Imag.*, vol. 6, pp. 163-165, 2015.

[3] S. Martin, and C. T. M. Choi, "Nonlinear electrical impedance tomography reconstruction using artificial neural networks and particle swarm optimization," *IEEE Trans. Magn.*, vol. 52, no. 3, Mar 2016, Art. no. 7203904.

[4] N. De Geeter, G. Crevecoeur, and L. Dupré, "A numerical study on conductivity estimation of the human head in the low frequency domain using induced current MR phase imaging EIT with multiple gradients," *IEEE Trans. Magn.*, vol. 49, no. 9, pp. 5004-5010, Sep 2013.

[5] L. Yang, S. Yang, S. L. Ho, and W. N. Fu, "An improved evolution strategy and its application to inverse scattering in microwave imaging," *IEEE Trans. Magn.*, vol. 51, no. 3, Mar. 2015, Art. no. 7202504.

[6] E. M. Haacke, L. S. Petropoulos, E. W. Nilges, and D. H. Wu, "Extraction of conductivity and permittivity using magnetic resonance imaging," *Phys. Med. Biol.*, vol. 36, no. 6, pp. 723-734, Jun. 1991.

[7] U. Katscher, *et al*, "Determination of electric conductivity and local SAR via B1 mapping," *IEEE Trans. Med. Imag.*, vol. 28, no. 9, pp. 1365-1374, Sep. 2009.

[8] V. L. Yarnykh, "Actual flip-angle imaging in the pulsed steady state: A method for rapid three-dimensional mapping of the transmitted radiofrequency field," *Magn. Reson. Med.*, vol. 57, pp. 192-200, Jan. 2007.

[9] E. Balidemaj, *et al.*, "CSI-EPT: a contrast source inversion approach for improved MRI-based electric properties tomography," *IEEE Trans. Med. Imag.*, vol. 34, no. 9, pp. 1788-1796, Sep. 2015.

[10] A. Arduino, L. Zilberti, M. Chiampi, and O. Bottauscio, "CSI-EPT in presence of RF-shield for MR-coils," *IEEE Trans. Med. Imag.*, in press. doi: 10.1109/TMI.2017.2665688.

[11] E. Balidemaj, *et al.*, "B1-based SAR reconstruction using contrast source inversion-electric properties tomography (CSI-EPT)," *Med. Biol. Eng. Comput.*, vol. 55, no. 2, pp. 225-233, Feb. 2017.

[12] A. Arduino, M. Chiampi, L. Zilberti, and O. Bottauscio, "Alternative approaches to magnetic resonance-based electric properties tomography and local specific absorption rate estimation," *IEEE Trans. Magn.*, vol. 53, no. 2, Feb. 2017, Art. no. 5100108.

[13] S. K. Lee, S. Bulumulla, and I. Hancu, "Theoretical investigation of random noise-limited signal-to-noise ratio in MR-based electrical properties tomography," *IEEE Trans. Med. Imag.*, vol. 34, pp. 2220-2232, Nov. 2015.

[14] Joint committee for guides in metrology, JCGM 101:2008, *Evaluation of measurement data—Supplement 1 to the 'Guide to expression of uncertainty in measurement'—Propagation of distributions using a Monte Carlo method*, BIPM, Paris, 2008.

[15] U. Katscher, D.-H. Kim, J. K. Seo, "Recent progress and future challenges in MR electric properties tomography," *Comput. and Math. Meth. in Med.*, vol. 2013, 2013.

[16] P. M. van den Berg, and A. Abubakar, "Contrast source inversion method: state of art," *Progr. Electromagn. Res.*, vol. 34, pp. 189-218, 2001.

[17] A. Christ, *et al.*, "The Virtual Family—development of surface-based anatomical models of two adults and two children for dosimetric simulations," *Phys. Med. Biol.*, vol. 55, no. 2, pp. N23-N38, Jan. 2010.

[18] IT'IS (2017). Database for thermal and electromagnetic parameters of biological tissues. [Online]. Available: https://www.itis.ethz.ch/database